Quantum Reservoir Computing for Hamiltonian Learning in Metal-Insulator Anderson Transitions

Author: Lucía Cortés Páez
*Facultat de Física, Universitat de Barcelona, Diagonal 645, 08028 Barcelona, Spain.**

Advisor: Pere Mujal Torreblanca
ICFO-Institut de Ciències Fotòniques, The Barcelona Institute of Science and Technology, 08860 Castelldefels, Spain.

Tutor: Bruno Juliá Díaz
Facultat de Física, Universitat de Barcelona, Diagonal 645 , 08028 Barcelona, Spain.

Abstract: This research investigates transport regimes in metal-insulator Anderson transition through Hamiltonian learning. Quantum reservoir computing is employed to estimate the stochasticity parameter in the Hamiltonian of the quasiperiodic kicked rotor, a model that displays Anderson transition in momentum space. The stochasticity parameter is key for classifying phase regimes, i.e., localized/insulator phase, delocalized/metalic phase, and critical phase, as well as qualitatively forecasting trajectory evolution. Thus, supervised machine learning that effectively maps input trajectories to their corresponding stochasticity parameter has been developed, highlighting the efficacy of quantum machine learning in analyzing quantum phenomena.

I. INTRODUCTION

Since the discovery of Anderson localization in 1958 [1], it has been known that disorder can localize quantum particles. In three-dimensional non-interacting disordered electron systems, this implies a phase transition, known as the Anderson transition, from a diffusive or metallic phase to an insulating or localized phase. This diffusive transport is suppressed due to destructive quantum interference introduced by the disorder of the system, leading to localization [2].

The original paper [1] and subsequent numerical simulations and experiments have confirmed Anderson localization in 1D in light waves, microwaves, electron gases, and matter-waves [3]. However, in three dimensions, the experimental observation of the Anderson transition remains challenging [4]. The quasiperiodical kicked rotor (QPKR) with three incommensurate frequencies, introduced in Refs. [5, 6], has proven to display the Anderson transition in momentum space, making it an effective tool for studying the metal-insulator phase regimes. This approach is also experimentally feasible, as demonstrated in experiments with cold atomic gas exposed to laser pulses [7].

In recent years, quantum machine learning (QML) has emerged as a promising field, attracting attention from both the scientific community and industry due to its potential to enhance computational speed, learning capacity, and efficiency [8]. One notable application of QML is time-series processing and forecasting. In the domain of physics, temporal evolutions are observed virtually everywhere, ranging from microscopic to macroscopic scales, and in both quantum and relativistic systems. Consequently, QML holds promise for catalyzing significant breakthroughs in physics.

Temporal tasks require continuous monitoring of data, and it is essential to preserve the sequential integrity of the data for effective processing. Quantum reservoir computing (QRC)[9] is a kind of recurrent neural network that is effective for this type of tasks [10, 11]. The motivation for using QRC stems from QML algorithms' ability to handle high computational complexity due to the utilization of Hilbert spaces, which facilitate the representation of quantum states in exponentially large dimensional spaces. This enables operations and information storage on a scale that classical systems cannot efficiently manage [12]. In addition, QRC is advantageous for model training due to its rapid, efficient linear fit process, avoiding high resource costs, and it allows for multitasking by applying different linear fits to the reservoir outputs [9, 13].

In this research, the metal-insulator Anderson transition has been studied by developing a supervised machine learning (SML) tool using spin-based QRC, capable of providing valuable information about the transport regimes in momentum space of a wave packet in the QPKR. The focal point of this study has been the estimation of the stochasticity parameter in the Hamiltonian of the QPKR (Hamiltonian Learning), by using a QRC consisting of a complex network of N randomly coupled qubits. Then the desired observables of the spins are obtained in the output layer, and through linear regression the weights of the outputs can be optimized to obtain the targeted function, i.e., the value of the stochasticity parameter. Thus, a SML model has been developed where inputting a trajectory in momentum space yields its stochasticity parameter. This parameter is of great significance as, given an experimental trajectory, it allows for classification into metal, critical, or insulator phases, thus gaining knowledge of the trajectory evolution in time.

*Electronic address: lcortepa7@alumnes.ub.edu

The paper is structured as follows: Section II reviews the dynamics of the QPKR, and the time dependence of transport regimes in momentum space. Section III describes the QRC and its functionality. Section IV presents the models for stochasticity parameter forecasting and the main results. Finally, the conclusions are in Section V.

II. DYNAMICS OF THE QUASIPERIODICAL KICKED ROTOR

In the following lines, the dynamics of the QPKR and transport regimes in the Anderson transition are explored, numerically recreating the experimental conditions used in the observation of metal-insulator transition with atomic matter waves from Ref. [7].

The QPKR can be described by the time-dependent, scaled, dimensionless Hamiltonian [7],

$$H(t) = \frac{p^2}{2} + K\cos(x) \times \sum_n \delta(t-n) \times \mathcal{K}(t) \tag{1}$$

with

$$\mathcal{K}(t) = 1 + \epsilon\cos(\omega_2 t + \theta_2) \times \cos(\omega_3 t + \theta_3), \tag{2}$$

where K is the stochasticity parameter, ω_i are the incommensurate frequencies, ϵ the modulation strength and θ_i the initial phases. The dynamics of the Hamiltonian in Eq.(1) are studied by solving the time-dependent Schrödinguer equation:

$$ik\frac{\mathrm{d}}{\mathrm{d}t}\psi(t) = H(t)\psi(t), \tag{3}$$

where k is the scaled Plank constant. To this aim, one considers the one-period evolution operator, also known as the period-1 Floquet operator [7]:

$$\hat{U} = \hat{U}_{kick}\hat{U}_{free} = e^{-\frac{1}{k}Kcos\hat{x}\mathcal{K}(t)}e^{-\frac{1}{2k}\hat{p}^2}. \tag{4}$$

This operator factorizes into the product of the kick operator phase and the free evolution phase. This is due to the $\delta(t-n)$ term in Eq.(1) as the evolution of the kinetic energy term is negligible during the kick[14]. The free evolution term is diagonal in momentum space, whereas the kick operator term is diagonal in position space. To switch to position space, the Fourier transform is applied. The wave-function $\psi_p(t)$ at time t can be obtained by applying successively $\hat{U}(t';t-1)$ for t' from 1 to t:

$$\psi(t) = \prod_{t'=1}^{t} \hat{U}(t';t'-1)\psi(x,t=0). \tag{5}$$

As we discuss in the following lines, it is particularly interesting to compute $\langle p^2(t)\rangle$:

$$\langle p^2(t_k)\rangle = \sum_{i=0}^{n} |\psi(p_i)|^2 p_i^2, \tag{6}$$

where n is the number of elements of our basis when we truncate the momentum space.

The $\langle p^2(t)\rangle$ trajectories define how wavepackets diffuse in momentum space:

$$\langle p^2(t)\rangle \sim \begin{cases} Dt & \text{delocalized/metal phase,} \\ \xi^2 & \text{localized/insulator phase,} \\ t^{2/3} & \text{critical phase,} \end{cases} \tag{7}$$

with ξ the localization length and $D = \frac{K^2}{2\hbar}$ the diffusion constant. In order to observe localization, disorder must be introduced to the system, i.e, $(k, \omega_2, \omega_3, \pi)$ must be incommensurate. This parameters have been set to $(2.89, 2\pi\sqrt{3}, 2\pi\sqrt{13}, \pi)$ according to [15]. The metal-insulator transition is observed in the (K, ϵ) plane. The larger K and ϵ, the smaller the disorder, leading to a diffusive regime. Ref. [4] has shown that $K = 4$, $\epsilon = 0.1$ is in the localized region, $K = 9, \epsilon = 0.8$ is in the diffusive region and the critical line is crossed at $K = Kc = 6.6$, $\epsilon = \epsilon_0 \approx 4.5$. Thus, by knowing the value of K and ϵ for a given trajectory $\langle p^2(t)\rangle$ it is possible to identify its phase regime as well as the trajectory evolution in time.

III. SPIN-BASED QUANTUM RESERVOIR COMPUTING

QRC is a machine learning approach that comprises three distinct layers[9]: the injection of the input into the dynamical system (quantum reservoir), the evolution of the reservoir under its natural dynamics, and the extraction of information from the reservoir through an output layer. This research uses a quantum reservoir consisting of a complex network of N randomly coupled qubits in a finite-dimensional Hilbert space of dimension 2^N, explored in [16]. It presents a dynamical phase transition from many-body localized (MBL) to an ergodic phase, that characterizes its performance[10]. Nonlinearity in the input-output map, which has proven to enchance computational performance, is introduced through the input encoding in one qubit [16].

A. Input encoding in one qubit

Various methodologies can be employed to introduce the input in the reservoir system. The method adopted in this study is the widely used technique [10, 16, 17] of input encoding in a single-qubit pure state:

$$|\psi_k\rangle = \sqrt{1-s_k}\,|0\rangle + \sqrt{s_k}\,|1\rangle\,, \tag{8}$$

where s_k is the normalized input, such that $s_k \in [0,1]$. Notice that the index k refers to the time step k in the time-series that is being processed. The input-state density matrix is:

$$|\psi_k\rangle\langle\psi_k| = \begin{pmatrix} 1-s_k & \sqrt{s_k(1-s_k)} \\ \sqrt{s_k(1-s_k)} & s_k \end{pmatrix} \tag{9}$$

such that the state of the system after the input injection is:

$$\rho_k = |\psi_k\rangle \langle\psi_k| \otimes \tilde{\rho}_{k-1}, \tag{10}$$

with $\tilde{\rho}_{k-1} = \mathrm{Tr}_1(\rho_{k-1})$. Tr_1 is the partial trace with respect to the first qubit (chosen arbitrarily), which operationally corresponds to discarding all information about the quantum state of the first qubit and feeding the input s_k to the reservoir.

B. Dynamic evolution of the reservoir

After introducing the input into the reservoir network, the system undergoes a unitary evolution governed by the Hamiltonian, $\hat{H}$ between steps of Δt.

$$\rho_k = e^{-i\hat{H}\Delta t} \left(|\psi_k\rangle \langle\psi_k| \otimes \tilde{\rho}_{k-1}\right) e^{i\hat{H}\Delta t}. \tag{11}$$

The choice of the Hamiltonian for the QRC is a significant one, as it directly impacts on the performance of the reservoir [10, 16]. The transverse-field Ising Hamiltonian considered here, which is analyzed in [10, 16, 17], has demonstrated high performance for nonlinear tasks:

$$\hat{H} = \frac{h}{2} \sum_{i=1}^{N} \hat{\sigma_i}^z + \sum_{i<j}^{N} J_{ij} \hat{\sigma_i}^x \hat{\sigma_j}^x, \tag{12}$$

where J_{ij} are the spin-spin couplings randomly generated from a uniform distribution in the interval $[-\frac{J_s}{2}, \frac{J_s}{2}]$, and h is the transversal magnetic field written in units of J_s. This external field, h, determines the dominance of the z-direction over the other directions.

C. Reservoir output: expectation values of observables

As explored in [16], the functional form of an expectation value of any observable $\hat{O}$ for the input encoding in a single-qubit pure state is:

$$\langle\hat{O}\rangle_k = \mathrm{Tr}(\hat{O}\rho_k^{(0)}) + s_k \mathrm{Tr}(\hat{O}\rho_k^{(1)}) + r_k \mathrm{Tr}(\hat{O}\rho_k^{(nl)}). \tag{13}$$

The observables have a term independent of s_k, a term proportional to s_k, and a nonlinear term, with $r_k = \sqrt{s_k(1-s_k)}$. For each model, a selection of observables are the QRC output.

D. Linear regression for the optimization of the output weights

The prediction of the targeted function, i.e. K, is achieved with a linear regression model by optimizing the weights of the output observable from the reservoir network with the Least Squares method [13]. The predictions, $\tilde{K}$, take the general form:

$$\tilde{K} = w_0 + \sum_{i=1}^{N} \left(w_{1,i} \langle\sigma_i^x\rangle + w_{2,i} \langle\sigma_i^y\rangle + w_{3,i} \langle\sigma_i^z\rangle\right). \tag{14}$$

The performance of the model can be quantified by the coefficient of determination:

$$R^2 = 1 - \frac{\sum_{i=1}^{L}(K_i - \tilde{K}_i)^2}{\sum_{i=1}^{L}(\bar{K} - K_L)^2}, \tag{15}$$

where L is the number of trajectories in a given dataset. If $R^2 = 1$, $\tilde{K}$ and K are perfectly correlated, meaning $\tilde{K} = K$. Conversely, if $R^2 = 0$, there is no correlation between K and $\tilde{K}$, and the predictions are fatal.

IV. STOCHASTICITY PARAMETER FORECASTING

The methodology for predicting the stochasticity parameter for the $\langle p^2(t)\rangle$ trajectories in different phase regimes and the performance of the considered models are detailed in the following subsections.

A. Obtention of trajectories in momentum space and QRC output observables

Initially, the $\langle p^2(t)\rangle$ trajectories were computed by numerically solving the time-dependent Schrödinger equation (3), as described in Section II. Each trajectory corresponds to specific values of K and ϵ. To analyze the different regimes —localized, delocalized, and critical— 500 $\langle p^2(t)\rangle$ trajectories were generated with K values and ϵ values quadratically distributed within the intervals $[4, 9]$ and $[0.1, 0.8]$, respectively. Each trajectory has 200 time steps t_k, i.e., 200 kicks. The representation of $\langle p^2(t)\rangle$ for different phase regions is shown in Figure 1.

We handle the different orders of magnitude taken by $\langle p^2\rangle$ in the different transport regimes by computing its logarithm. In addition, scaling the values to $[0, 1]$ ensures that all features contribute equally, preventing dominant values and improving numerical stability.

The dataset contains 500 $\langle p^2(t)\rangle$ trajectories scaled to $[0, 1]$, where each trajectory spans 200 s_k values. s_k refers to the value of $\langle p^2(t_k)\rangle$ for a time step t_k in a trajectory. Additionally, each trajectory in the dataset is labeled with the corresponding K and ϵ values, that are used in the SML with QRC.

By iteratively feeding s_k to the QRC, each trajectory from the initial dataset is represented by $3N$ time series of 200 time steps, corresponding to $\langle\sigma_x^{(1)}\rangle, \langle\sigma_y^{(1)}\rangle, \langle\sigma_z^{(1)}\rangle, \ldots, \langle\sigma_x^{(N=8)}\rangle, \langle\sigma_y^{(N=8)}\rangle, \langle\sigma_z^{(N=8)}\rangle$. This provides a richer dataset with more information about the $\langle p^2(t)\rangle$ trajectories, which can be highly useful for predicting K. By concatenating each $\langle\sigma_j^{(i)}\rangle$, a

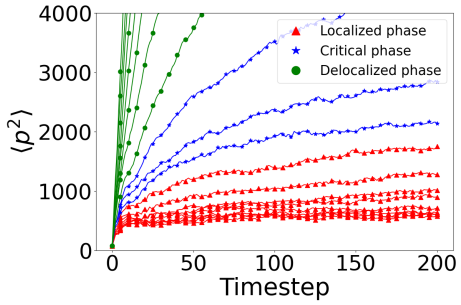

FIG. 1: Representation of $\langle p^2(t) \rangle$ for different phase regions. The delocalized phase exhibits a diffusive behavior of the wavepacket, indicated by the green trajectories that increase linearly over time. The localized phase, represented by the red trajectories, shows saturation to a finite value due to quantum interference. The blue trajectories, which are neither strictly linear nor saturated, correspond to the critical phase associated with the metal-insulator Anderson transition.

dataset of dimensions $M \times 3NT$ is obtained. Here, M denotes the number of trajectories to be analyzed, set to $M = 500$; T represents the number of time steps of each trajectory, set to $T = 200$; and N is the number of qubits in the reservoir network, set to $N = 8$. Therefore, the overall dataset size is 500×4800. This dataset is split into a Training Set (70%) and a Testing Set (30%). However, fitting this dataset into Eq (14) results in a vast number of free parameters, i.e., an overfitting of the model. This leads to extremely good performance during training ($R^2 = 1$), but poor generalization during testing ($R \ll 1$). To address this issue, the dataset size was reduced by summing each direction for all qubits, resulting in a dataset of $(M \times 3T) = (500 \times 600)$. Here, the sigmas are defined as: $\langle \sigma_j \rangle = \sum_{i=1}^{N} \langle \sigma_j^{(i)} \rangle$ with $j = x, y, z$. This data was further reduced using various procedures, leading to different predictive models.

B. Performance of predictive models

Model 1 incorporates contributions from the x, y, and z directions, i.e., $\langle \sigma \rangle = \sum_{j=x,y,z} \langle \sigma_j \rangle$. Model 2, Model 3, and Model 4 include only the $\langle \sigma_x \rangle$, $\langle \sigma_y \rangle$, and $\langle \sigma_z \rangle$, respectively. The hyperparameter h has been set to $h = 10$ and $h = 1$ as these values yield good reservoir performance [10].

For $h = 1$ (Figure 2), the QRC model shows exceptional prediction accuracy, particularly when integrating all observables ($\langle \sigma \rangle$), achieving $R^2 = 0.997$. This very high correlation is supported by the absolute error histogram, with most errors close to zero.

At $h = 10$ (Figure 3), there is a notable decline in accuracy for $\langle \sigma_x \rangle$ and $\langle \sigma_y \rangle$ ($R^2 = 0.65$ and 0.54), while $\langle \sigma_z \rangle$ remains high ($R^2 = 0.97$). The combined model at $h = 10$ achieves $R^2 = 0.990$, indicating that including all observables increases the capability of the model and mitigates performance issues seen in individual directions.

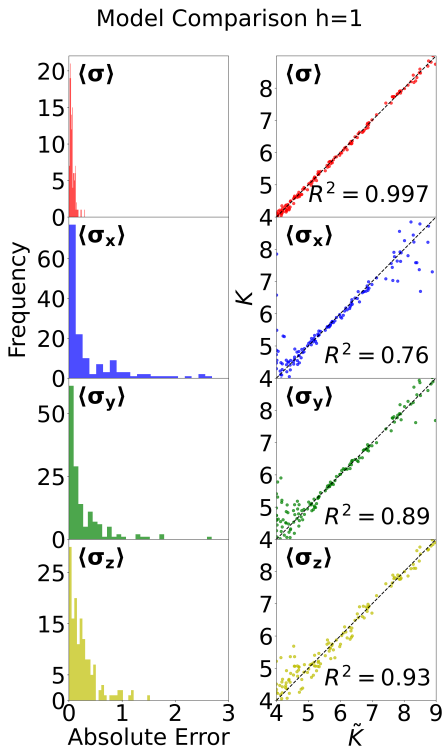

FIG. 2: Comparison of models for predicting the stochasticity parameter K using different observables $\langle \sigma_x \rangle$, $\langle \sigma_y \rangle$, $\langle \sigma_z \rangle$. The histograms display the absolute error distribution, while the scatter plots show the predicted $\tilde{K}$ versus the actual K with corresponding R^2 values, indicating the models' performance. The magnetic field hyperparameter is $h = 1$.

These trends align with theoretical expectations about the QRC's sensitivity to h explored in [10]. Lower h values in the ergodic phase regime enhance contributions from $\langle \sigma_x \rangle$ and $\langle \sigma_y \rangle$, creating a more balanced and accurate model. In contrast, higher h values increase the influence of $\langle \sigma_z \rangle$, reducing performance in $\langle \sigma_x \rangle$ and $\langle \sigma_y \rangle$. Overall, optimal performance is achieved at $h = 1$, emphasizing the importance of balancing contributions from all directions.

V. CONCLUSIONS

This research successfully applied QRC for Hamiltonian Learning in the metal-insulator Anderson transition using the QPKR model. We developed a QRC that accurately estimates the stochasticity parameter K, enabling precise classification of phase regimes. Analyzing $\langle p^2(t) \rangle$ trajectories for various K and ϵ values confirmed distinct behaviors in different phase regimes: linear increase in the delocalized phase, saturation in the localized phase, and $t^{\frac{2}{3}}$ behavior in the critical phase.

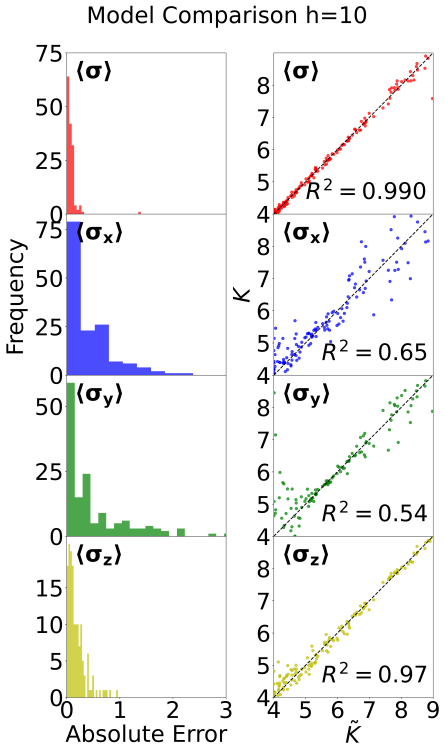

FIG. 3: Comparison of models for predicting the stochasticity parameter K using different observables $\langle\sigma_x\rangle$, $\langle\sigma_y\rangle$, $\langle\sigma_z\rangle$. The histograms display the absolute error distribution, while the scatter plots show the predicted $\tilde{K}$ versus the actual K with corresponding R^2 values, indicating the models' performance. The magnetic field hyperparameter is $h = 10$.

QRC models exhibited high efficiency and accuracy, leveraging the high-dimensional Hilbert space for enhanced performance. The input encoding in a single pure state and dynamic reservoir evolution governed by the transverse-field Ising Hamiltonian proved effective, and the model showed good generalization capability, with satisfactory R^2 values during testing, reaching a maximum performance of $R = 0.997$. QRC sensitivity to the hyperparameter h was significant, with optimal performance in the ergodic phase at $h = 1$.

This research highlights the practical and efficient utility of QRC in quantum phase classification and Hamiltonian Learning. Future research can explore alternative QRC architectures with different input encodings, and extending the approach to larger and chaotic quantum systems where numerical methods are required, which shows the potential of QRC and QML in advancing our understanding of phase transitions and quantum phenomena, potentially leading to significant breakthroughs in the field.

Acknowledgments

I would like to express my gratitude to Dr. Pere Mujal and Dr. Bruno Juliá for their guidance and support throughout this research, as well as thanking Dr. Antonio Acín for welcoming me into the Quantum Information Theory Group at ICFO. I also wish to thank my parents and family for their unwavering encouragement and to Àlex for his constant support and inspiration.

[1] P. W. Anderson. Absence of diffusion in certain random lattices. *Phys. Rev.*, 109:1492–1505, 1958.
[2] E. Abrahams et al. *Scaling Theory of Localization: Absence of Quantum Diffusion in Two Dimensions*, pp. 516–518. 2018.
[3] J. Billy et al. Direct observation of anderson localization of matter waves in a controlled disorder. *Nature*, 453(7197):891–894, 2008.
[4] J. Chabé et al. Experimental observation of the anderson metal-insulator transition with atomic matter waves. *Physical Review Letters*, 101(25), 2008.
[5] G. Casati et al. Anderson transition in a one-dimensional system with three incommensurate frequencies. *Phys. Rev. Lett.*, 62:345–348, 1989.
[6] D. Shepelyansky. Some statistical properties of simple classically stochastic quantum systems. *Physica D: Nonlinear Phenomena*, 8(1):208–222, 1983.
[7] G. Lemarié et al. Observation of the anderson metal-insulator transition with atomic matter waves: Theory and experiment. *Phys. Rev. A*, 80:043626, 2009.
[8] F. Phillipson. Quantum machine learning: Benefits and practical example. 2020.
[9] P. Mujal et al. Opportunities in quantum reservoir computing and extreme learning machines. *Advanced Quantum Technologies*, pp. 2100027, 2021.
[10] R. Martínez-Peña et al. Dynamical phase transitions in quantum reservoir computing. *Phys. Rev. Lett.*, 127:100502, 2021.
[11] J. Nokkala et al. Gaussian states of continuous-variable quantum systems provide universal and versatile reservoir computing. *Communications Physics*, 4(1), 2021.
[12] F. Arute et al. Quantum supremacy using a programmable superconducting processor. *Nature*, 574(7779):505–510, 2019.
[13] P. Mujal. Quantum reservoir computing for speckle disorder potentials. *Condensed Matter*, 7(1), 2022.
[14] M. Lepers et al. Kicked-rotor quantum resonances in position space. *Physical Review A*, 77(4), 2008.
[15] Y. Guo et al. Observation of many-body dynamical localization, 2023.
[16] P. Mujal et al. Analytical evidence of nonlinearity in qubits and continuous-variable quantum reservoir computing. *Journal of Physics: Complexity*, 2(4):045008, 2021.
[17] K. Fujii and K. Nakajima. Harnessing disordered-ensemble quantum dynamics for machine learning. *Phys. Rev. Appl.*, 8:024030, 2017.